



Simulation of damage and failure processes of thermal barrier coatings subjected to a uniaxial tensile load



Linlin Wang, Qunbo Fan^{*}, Yanbo Liu, Guoju Li, Hongmei Zhang, Quansheng Wang, Fuchi Wang

National Key Laboratory of Science and Technology on Materials under Shock and Impact, School of Materials Science and Engineering, Beijing Institute of Technology, Beijing 100081, China

ARTICLE INFO

Article history:

Received 18 May 2015

Received in revised form 7 July 2015

Accepted 20 July 2015

Available online 23 July 2015

Keywords:

Thermal barrier coatings

Microstructures

Delamination

Finite elements

ABSTRACT

The tensile bond strength of thermal barrier coatings (TBCs) is an important criterion in evaluating the quality of coatings, which depends significantly on the coatings' complex microstructures. In the current study, a three-dimensional (3D) microscopic structural model reflecting the actual interface morphology and pore distribution of TBCs is built using microcomputer tomography (micro-CT). The model is then applied to investigate the 3D spatial evolution processes of damage and failure under uniaxial tension using FE techniques. To validate the numerical simulation results, the tensile responses of the TBCs are measured and a follow-up quantitative description of the tensile fracture morphology is obtained with a 3D surface profiler. The simulation results are in good agreement with the experimental data. Our simulation results show that the local stress concentration induces two types of crack sources located either at the top coat (TC)/bond coat (BC) interface or along the pore boundaries; as the load increases, only the microcracks at the interface amalgamate and begin to form a primary crack; then the primary crack propagates rapidly horizontally along the interface, eventually inducing an undulating fracture morphology.

© 2015 Elsevier Ltd. All rights reserved.

1. Introduction

Thermal barrier coatings (TBCs) applied by atmospheric plasma spraying (APS) are widely used for hot-section blades in gas turbine engines [1–3]. Such coatings can provide protection for the metallic substrate, which results in an improved component durability [4–6]. Increased efficiency can be achieved by allowing an increase of the turbine inlet temperatures. APS TBCs comprise metal and ceramic multilayers. The ceramic layer, normally yttria-stabilized zirconia (YSZ), is used as a top coat (TC) and it provides thermal insulation, whereas the metal layer, called the bond coat (BC), is typically made from an MCrAlY alloy (where M stands for Fe, Ni, Co, or a combination of these elements). The BC provides adherence for the ceramic TC [7].

As we all know, the service life of TBCs is typically limited by spallation and delamination of the ceramic coatings [8]. For the past few years, many different types of failure modes leading to TBC spallation have been studied in laboratory experiments, and the most commonly used testing methods are tension [9–11] and bending tests [12,13]. These studies emphasize that the delamination failure of top coats normally results from the initiation and propagation of cracks either at the bottom of the TC layer or near the TC/BC interface, which severely limits the application of TBCs [14]. However, it is difficult to track or observe the crack propagation processes in real-time using the current experimental techniques. Therefore, to have a better understanding of

the intrinsic failure mechanisms in TBC systems, numerical simulation methods with a variety of finite element models have been developed [15]. In most of the earlier works, a two-dimensional (2D) or three-dimensional (3D) sinusoidal wave profile has been chosen as a simplification to represent the TBC interface [16–26]. A crack propagation model was proposed by Ranjbar et al. [16] and Bialas [17] to analyze the stress distribution in TBCs using a 2D wave profile to represent the TC/BC interface. Ranjbar used both uniform and non-uniform amplitudes to represent the wave profile and an inhomogeneous top coat layer with an artificial lamellar structure. It was concluded that the cracking depends mainly on the interface morphology. Failure mechanisms were analyzed by Evans [20] with the help of a 2D finite element model representing the interface as a sine wave profile. Similarly, lifetime prediction models were made by Vassen et al. [21], Shen et al. [22], and He et al. [23] based on the growth of delamination cracks using a 2D sine wave profile to model the interface. Recently, Jinnestrand et al. [24] developed a model using a 3D sine wave profile to represent the interface to analyze the stress distribution.

However, a simplified roughness profile might not lead to precise predictions as it does not incorporate the actual complex surface topography created by plasma spraying. An attempt was made by Shen [7] and Bolelli [27] to overcome this limitation by generating a finite element geometric model of TBCs based on an actual 2D microstructural image. Using this method, damage accumulation and microcrack growth were clearly observed during the simulation. However, no additional 3D information of the microstructure and the failure mechanisms could be obtained because of the 2D modeling method. Gupta [28]

^{*} Corresponding author.

E-mail address: fanqunbo@bit.edu.cn (Q. Fan).

Table 1
Basic operating parameters of plasma spraying.

	Primary gas, Ar (SCFH)	Secondary gas, H ₂ (SCFH)	Carrier gas, Ar (SCFH)	Electric current (A)	Powder rate (RPM)	Spraying distance (mm)
Bond coat	120	20	10	700	2	75
Top coat	75	45	8	850	5	75

represented the 3D TC/BC interface successfully by using actual BC surface topographies scanned with a white-light interferometry technique before spraying the top coat layer. However, the representation of pores and microcracks with irregular shapes and distributions, which influence the mechanical behavior of the coatings dramatically, cannot be taken into account in this method [29,30]. In this case, some new approaches were developed to relate 3D pores and crack interconnections [31–34]. In Amsellem's study [32], for example, X-ray micro-tomography (XMT) was performed at the European Synchrotron Radiation Facility (ESRF) using beamline ID19 (a high-resolution diffraction topography beamline) to reconstruct the microstructures of plasma-sprayed alumina.

However, up to the present time, existing models are not yet sufficiently mature to allow reliable prediction of the tensile bond strength of TBCs. In this study, a 3D microscopic structural model of TBCs that reflects the actual interface morphology and pore distribution was built using common laboratory microcomputer tomography (micro-CT) for the first time. This method is helpful for characterizing tension delamination properties and for revealing the failure mechanisms in TBC systems. The crack initiation and propagation path in 3D space were taken into account and the modeling results, including tensile bond strength and fracture surface morphology, were investigated and quantitatively compared with the observed experimental results.

2. Experimental methods and characterization

2.1. Materials and specimen

The thermal barrier coatings investigated in this study were a ceramic/metal bilayer system prepared using a Praxair SG-100 plasma spray gun (Praxair Inc., Danbury, Connecticut, USA), and the basic operating parameters used for deposition of the coatings are listed in Table 1. Prior to spraying, the surface of GH4169 superalloy substrates with thicknesses of 10 mm and diameters of 25 mm were cleaned with alcohol and then NiCoCrAlY bond coats (CO-210 alloy powder, Praxair Inc., USA) with thicknesses of 100 μm were plasma-sprayed onto the substrate surfaces. Subsequently, nanostructured ceramic top coats produced using 8 wt.% yttria-stabilized zirconia powder were applied on the bond coats with an 8 mm nozzle. The thicknesses of the top coat layer were

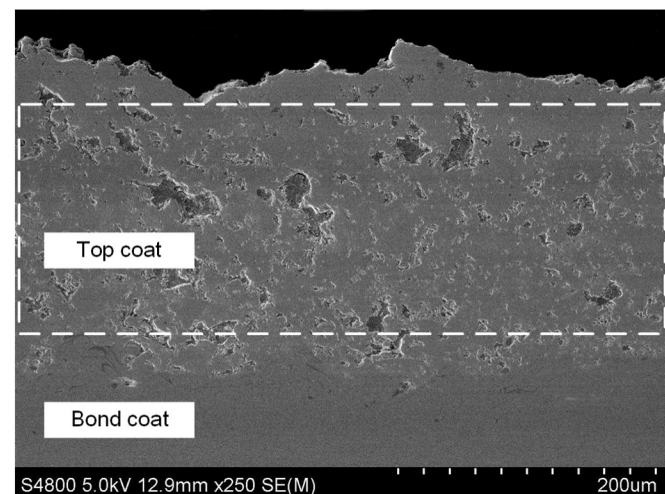


Fig. 1. SEM image of the cross-sectional microstructures of a TBC.

approximately 150 to 160 μm. Fig. 1 shows a typical scanning electron microscope (SEM) image of the cross-sectional microstructures of a TBC for the coating porosity measurement; the white box shows the area used for statistical analysis. In this study, a total of 20 random SEM images from four different specimens were employed, and the average final porosity for the TBCs was $9.4 \pm 0.1\%$.

2.2. Tension delamination experiment

One of the simplest and most widely used methods to determine the bond strength of an interface is the tension delamination experiment. The specimens for such an experiment are bonded on both sides onto steel tension bars using a commercial epoxy (Araldite AW106/HV953). The specimens are then cured at 150 °C for 20 min. A schematic of a specimen prepared in this manner is shown in Fig. 2. According to the Chinese National Standard GB/T 8642-2002, the tensile bond strength, R_H is calculated by Eq. (1):

$$R_H = \frac{F_m}{S} \quad (1)$$

where F_m is the maximum loading force; S is the cross-sectional area of TBC specimen.

Ten TBC specimens were tested in this study and their responses were reasonably consistent. Ten TBC specimens were tested in this

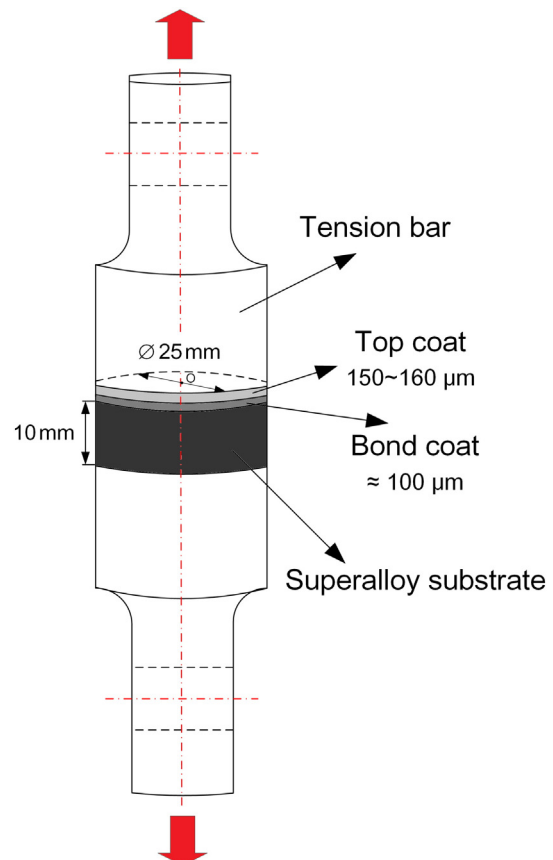


Fig. 2. Schematic of the tension specimen with dimensions.

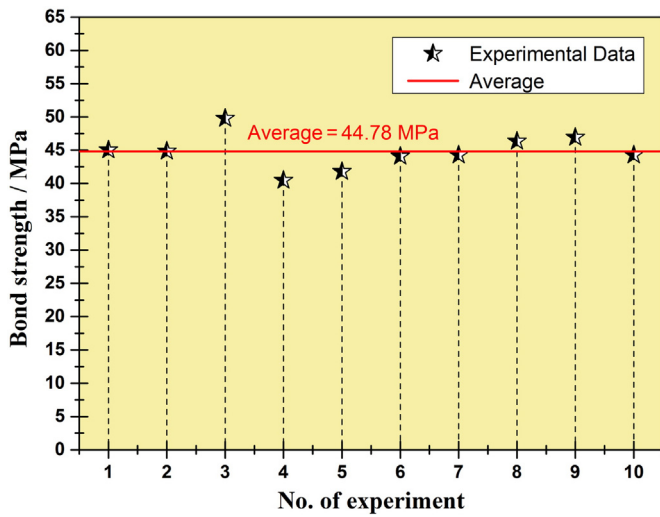


Fig. 3. Tensile bond strengths from ten tension experiments.

study and their responses were reasonably consistent, as shown in Fig. 3. The average tensile bond strength of the TBCs was found to be 44.78 MPa.

Fig. 4 shows the tension fracture surface of a TBC specimen obtained after the tension experiment, where both the exposed bond coat and the adherent top coat are clearly visible. It is apparent that the fracture path undulates and that it is always near or at the TC/BC interface.

3. Finite element modeling and simulation methods

To understand and explain the experiment results and the underlying failure mechanisms in the TBC system, finite element (FE) numerical simulations were performed using a 3D model based on the actual microstructures of the plasma-sprayed TBCs in order to simulate crack propagation during the tension experiment.

3.1. 3D finite element model based on the microstructures of TBCs

3.1.1. X-ray tomography and 3D reconstruction

One of the most novel methods for building a 3D model by accurately capturing actual microstructures is micro-CT, which is based on X-ray tomography. In X-ray tomography, an X-ray beam is directed onto a sample and the transmitted beam is recorded onto a detector. The resulting image is the projection of a volume in a 2D plane. In this study, however, considering the X-ray transmission capability for micro-CT and the high density of ceramic and bond coats, a small cylindrical TBC sample with dimensions of $\Phi 0.5 \text{ mm} \times 1 \text{ mm}$ was employed to characterize the microstructures. To prepare such a sample, atmospheric plasma was sprayed onto a prefabricated stepped substrate sample using the same operating parameters listed in Table 1. The final scanning sample was obtained by cutting off the bottom cylinder, as shown in Fig. 5.

Subsequently, the small cylindrical TBC sample was scanned using a high-resolution desktop micro-CT (Sky-Scan 1172) system [35]. A collimated X-ray beam (81 kV and 124 μA) penetrated the sample and the transmitted X-rays were collected using a charge-coupled device (CCD)-based detector. Tomography was carried out with a high voxel definition, i.e., $1.49 \times 1.49 \times 1.49 \mu\text{m}$. In this study, 281 transmission X-ray images were obtained while rotating the sample between 0° and 180° , which were then converted into slice images with different directions through the software NRecon. Subsequently, 170 high-resolution slice images of the regions of interest (ROI, $100 \times 100 \mu\text{m}$) in the z-direction (see Fig. 6) were reconstructed into a 3D image model ($100 \times 100 \times 253 \mu\text{m}$) by the Simpleware commercial package [36], which offers an extensive selection of image-processing tools to assist the user in visualizing and segmenting ROIs [37]. Fig. 6 shows a schematic of the TBC 3D model specification. It can be seen that pores and defects with irregular shapes and distributions exist inside the ceramic layer or at the TC/BC interface, which is similar to the microstructure detected by SEM. It should be mentioned, however, that due to the limited resolution of transmission X-ray images, interfaces between ceramic lamellae cannot be identified, and they were ignored in our simulation. Fortunately, the effects of the particle interfaces on the

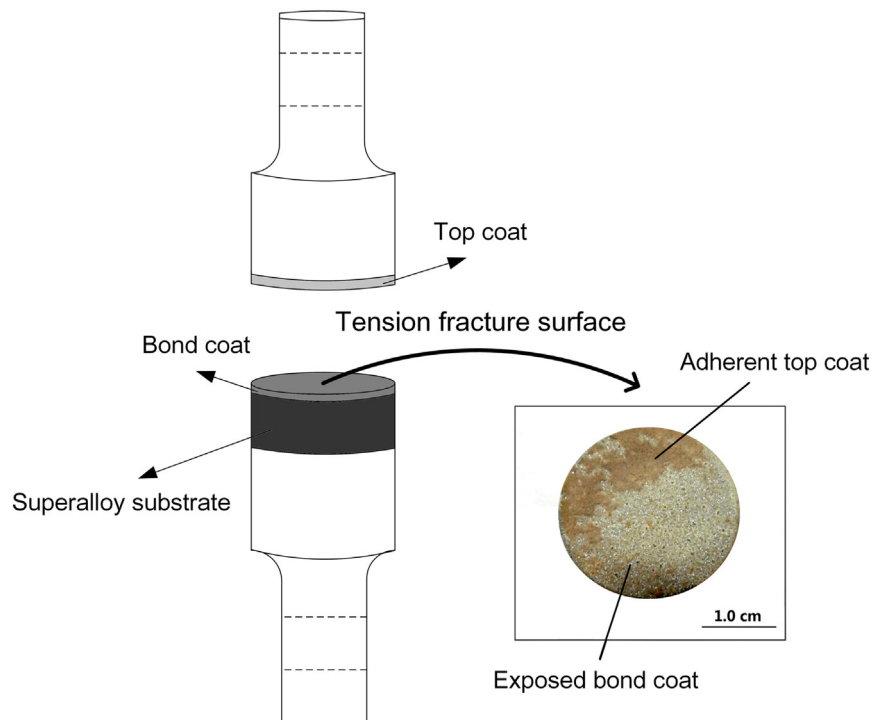


Fig. 4. Tension fracture surface of the specimen.

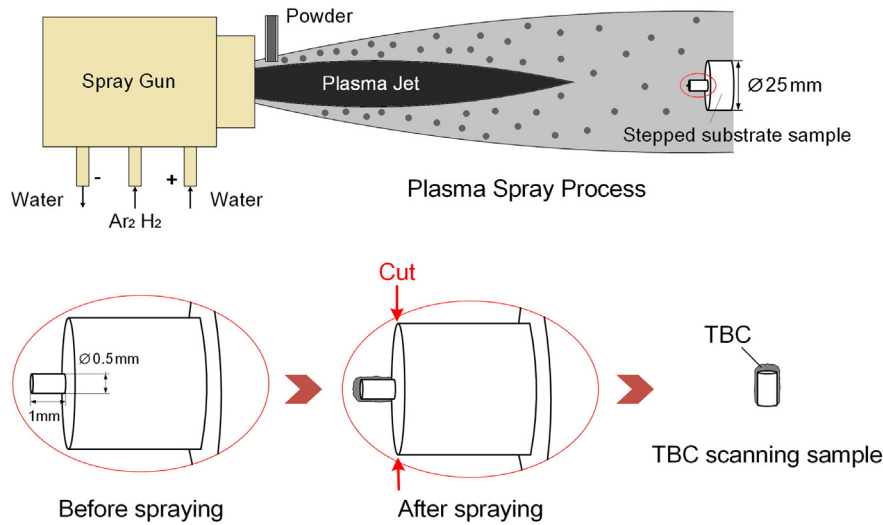


Fig. 5. Preparation of the small cylindrical sample for X-ray tomography.

stresses and crack propagation are negligible. For example, Wang [38] and Han [39] ignored the particle interfaces inside the top coat and successfully predicted the micromechanical and thermal response behavior of an actual coating. According to the statistical results of pore volume inside the top coat, the porosity of the ceramic coating for the TBC FE model was calculated to be 9.48%, which is consistent with the value obtained by SEM image analysis given in Section 2.1.

3.1.2. Mesh generation

The image model was then imported to the ScanFE module, which provides a robust approach for converting 3D image data into a volumetric mesh. In this study, solid elements were used and a 3D finite element model with mixed tetrahedral/hexahedral meshes was generated. A characteristic of such meshing is that it is highly dense and smooth at the interfaces, which allows us to outline the pore boundaries and the TC/BC interface morphology precisely, as shown in Fig. 7. Nodes

at the interface are shared with both the top coat and bond coat. In this case, the final model contained 807,480 tetrahedral elements and 612,393 hexahedral elements. The built FE model was then exported to the ANSYS LS-DYNA software for numerical analysis.

3.2. Boundary and loading conditions and material properties

Because the residual stresses in TBCs induced by plasma spraying are known to be only on the order of 3–5 MPa [19,40], the TBCs were considered to be stress-free at the beginning of the tension experiment. To obtain the tensile bond strength of the TBCs along the spraying direction, a changing stress condition was applied on plane $z = H$ in the z -direction by prescribing the quasi-static normal stress σ with a constant rate of 1 MPa/s, as shown in Fig. 7. In addition, the displacements of nodes on plane $z = 0$ were fixed. The nodes on plane $x = 0$ were free to displace in the plane, but they were all constrained to have the same

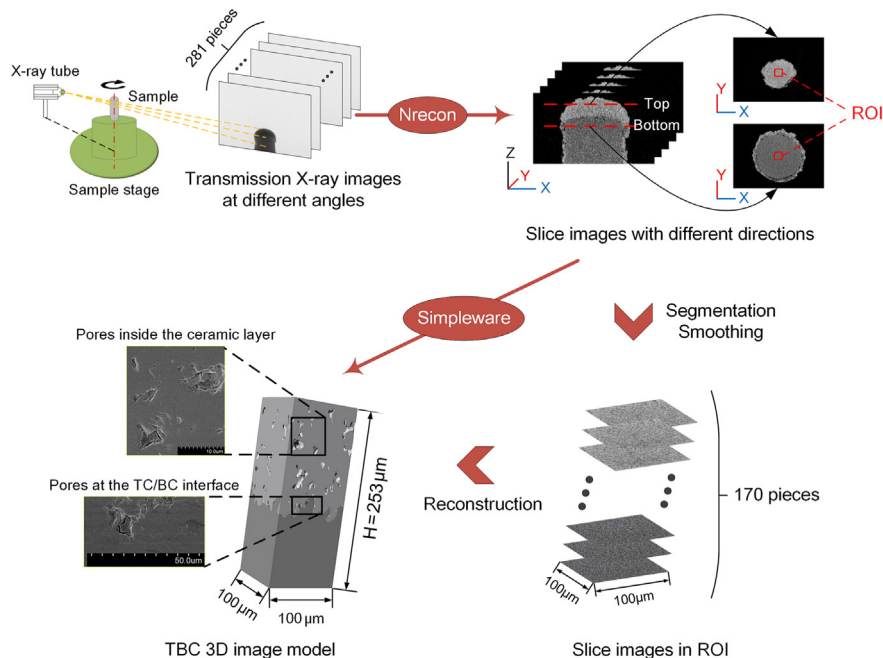


Fig. 6. Schematic of the TBC 3D model specification.

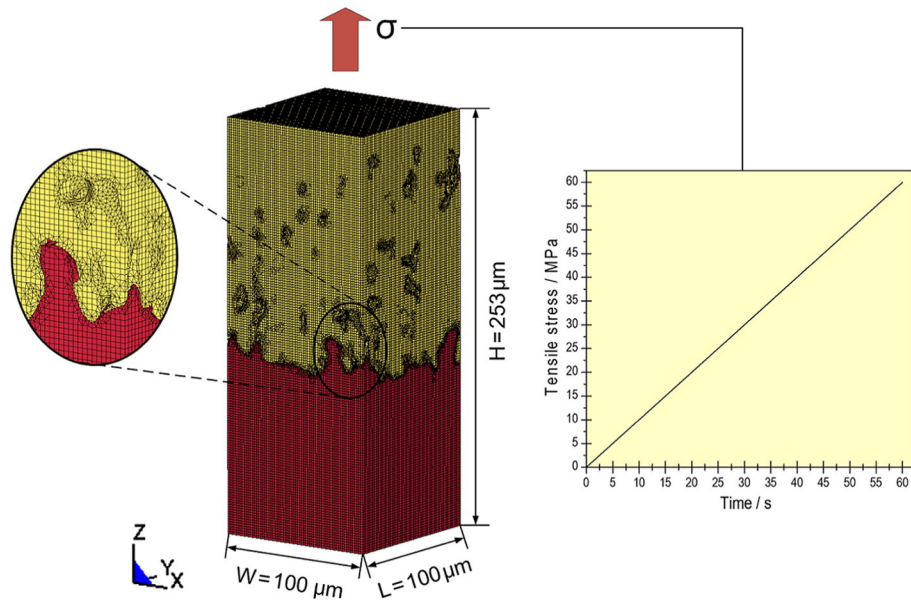


Fig. 7. 3D finite element model and the external tensile stress curve.

normal displacement “ u ” during the deformation in order to maintain a flat surface. The nodes on planes $x = L, y = 0, y = W$ were defined in a similar way, as shown in the following Eqs. (1)–(4), respectively.

$$u(0, y, z) = u(0, \cdot, \cdot, \cdot, 0) \quad (2)$$

$$u(L, y, z) = u(L, \cdot, \cdot, \cdot, 0) \quad (3)$$

$$v(x, 0, z) = v(0, \cdot, \cdot, \cdot, 0) \quad (4)$$

$$v(x, W, z) = v(0, W, 0) \quad (5)$$

where L, W , and H are the length, width, and height of the model, respectively; v is the displacement in the y -direction.

In our simulation, a linear elastic model was used to characterize the brittle behavior of YSZ (top coat) and the maximum tensile stress was defined as the failure criterion. The failure value was measured by our research group using the uniaxial compression Brazilian test, which is generally employed to acquire the tensile strength of the brittle materials indirectly [41]. The test method details can be found in the literature [7]. An elastic–plastic model was chosen to model NiCoCrAlY (bond coat). The properties of the two materials are listed in Table 2. During the simulation, the element that satisfied the failure criterion was deleted immediately from the model so the crack initiation and propagation of the TBCs would be observable.

4. Results and discussion

4.1. Comparative analysis of experimental and simulation results

4.1.1. Tensile bond strength

In FE analysis, the internal energy of the model due to the elastic–plastic deformation of the elements can be recorded. Fig. 8 shows the internal energy versus time curve of the whole 3D FE model, together

Table 2
Material properties used in the model.

	Young's modulus E (GPa)	Poisson's ratio ν	Yield stress σ_y (MPa)	Failure stress σ_f (MPa)
Top coat	80	0.26	–	215
Bond coat	200	0.30	426	–

with those of the individual top coat and bond coat throughout the entire process of uniaxial tension. It should be clear that elastic deformation of the top coat accounts for most of the energy absorption, about 73% of the whole model. After the internal energy of the whole model reaches its peak value at $t = 44.4$ s, it decreases rapidly because many elements of the TC layer have been deleted, and thus the stored internal energy of the failed elements is released. The external tensile stress at the time of 44.4 s (see Fig. 7) corresponding to the peak energy was chosen as the tensile bond strength of the TBC, i.e., 44.4 MPa, which is in good agreement with the statistical experimental result (44.78 MPa) reported in Section 2.2.

4.1.2. Tensile fracture morphology

A macroscopic visual inspection of the tension fracture surface of the TBC specimen (see Fig. 4) reveals that the fracture path is near or at the TC/BC interface, resulting in an undulating fracture morphology. However, a more detailed description of the tensile fracture morphology was obtained with a MicroXAM-100 Optical Surface Profiler (Profilometer), where quantitative parameters that characterize the topography of the fracture surface can also be obtained. The geometrical shape of a selected section of the tested fracture surface

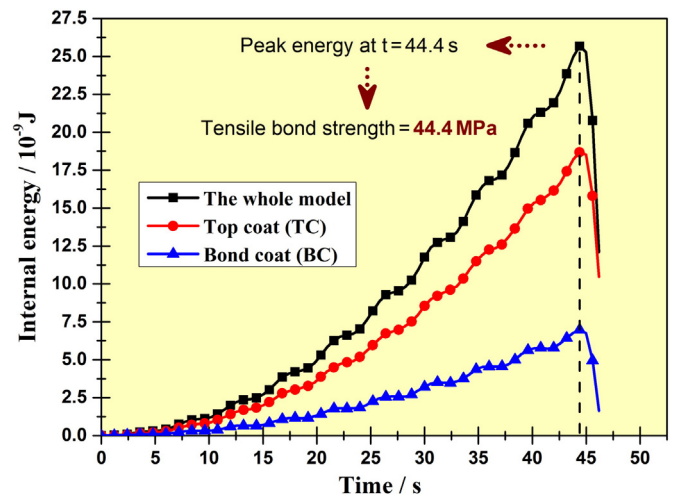


Fig. 8. Internal energy–time curve of the whole model and the individual top coat and bond coat.

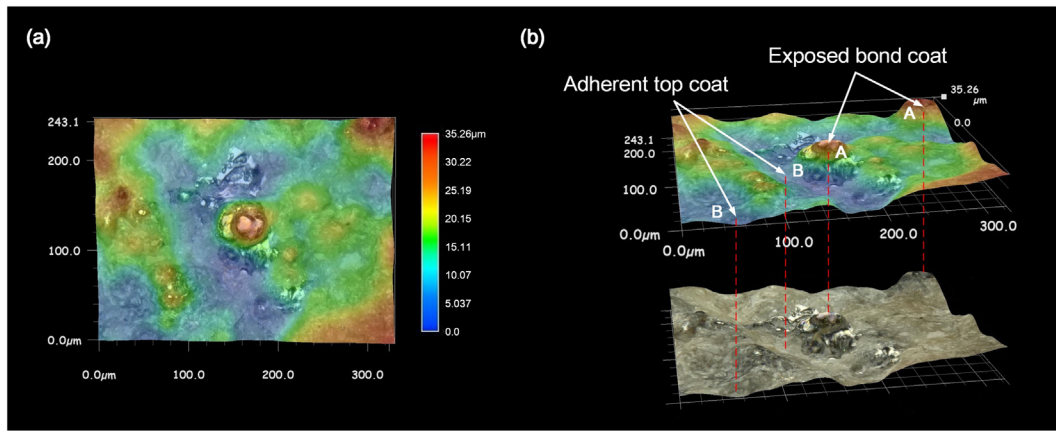


Fig. 9. Fracture morphology obtained by an optical profilograph: (a) 2D isometric image and (b) 3D topographical map.

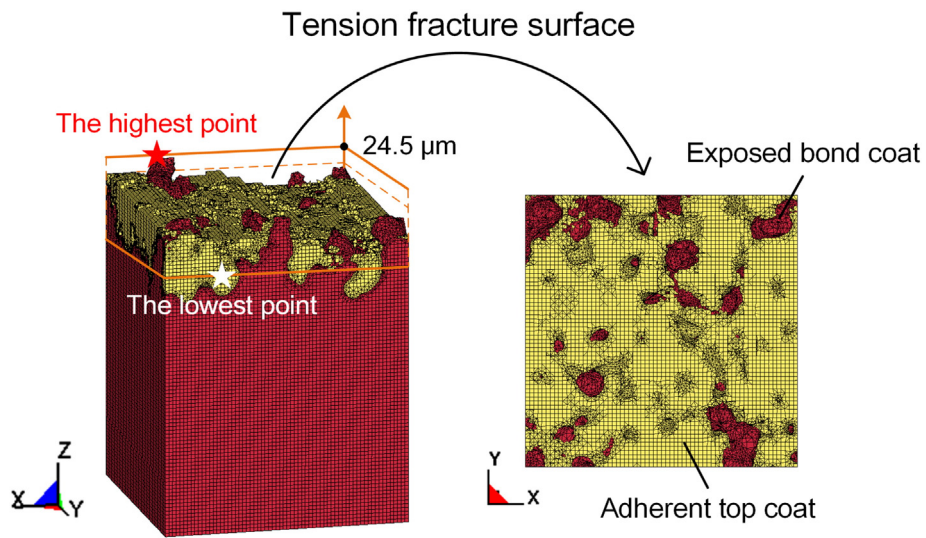


Fig. 10. 3D geometric morphology of the tension fracture surface.

(300.0 × 243.1 μm) is represented by a 2D isometric image and a 3D topographical map, as shown in Fig. 9(a) and (b), respectively. The results show that the convex sections (labeled as “A”) correspond to the

exposed bond coat, whereas the concave areas (labeled as “B”) correspond to the adherent top coat, and the difference in height between them is approximately 20–35 μm.

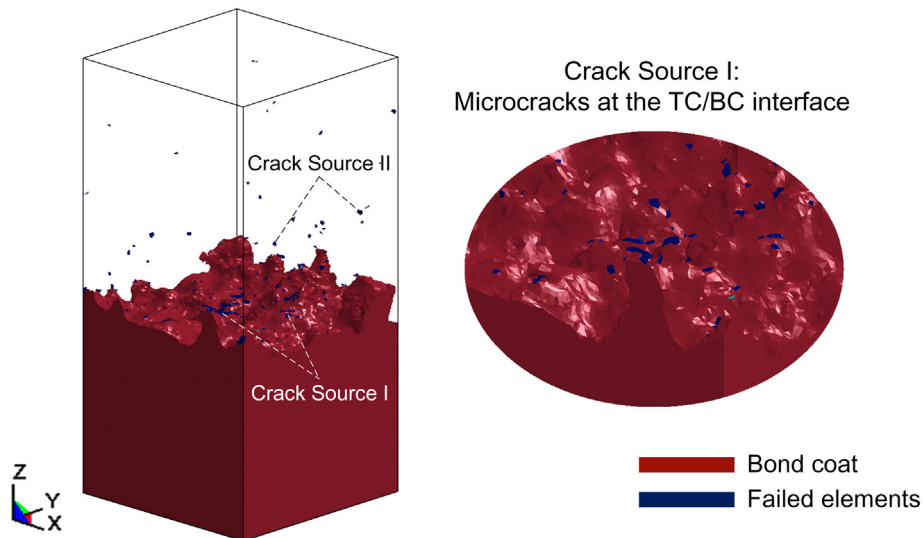


Fig. 11. The damage picture of the top coat at $t = 40.0$ s. Crack Source I: microcracks at the TC/BC interface.

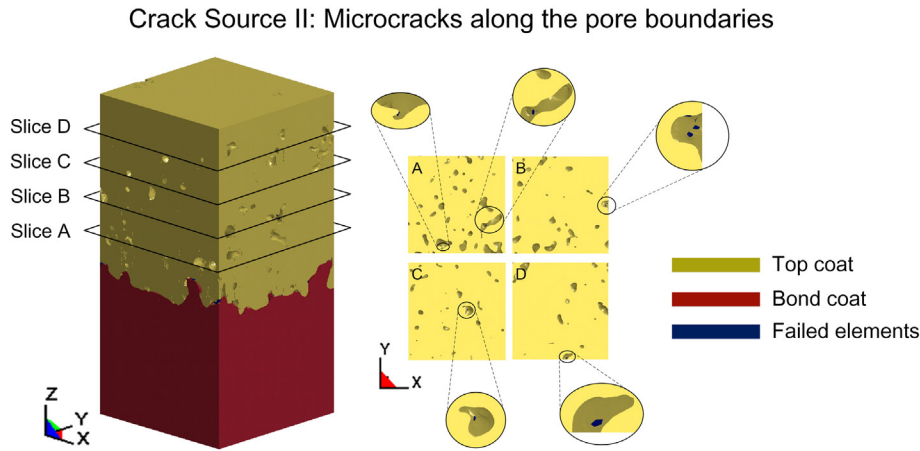


Fig. 12. Damage picture of the top coat at $t = 40.0$ s. Crack Source II: microcracks along the pore boundaries.

Similarly, simulation results for the TBC FE model, which characterizes the 3D geometric morphology of the fracture surface together with an additional scale, are presented in Fig. 10, and the distance between the lowest and the highest point of the fracture surface is $24.5 \mu\text{m}$, which is in good agreement with the available experimental data. From the overhead view of the tension fracture surface, one can conclude that crack propagation occurs both within the ceramic layer and at the TC/BC interface. The exposed bond coat and the adherent top coat show a perfect match with the observed experimental results shown in Fig. 4. Therefore, the methodology developed in our present work is reliable for studying the tension delamination properties and the failure mechanisms in TBC systems.

4.2. Coating delamination and failure analysis

This section discusses the underlying mechanisms of crack initiation, crack propagation, and final spallation of TBC subjected to a uniaxial tensile load.

4.2.1. Initiation of multiple crack sources

Fig. 11 shows the damage stereogram of the top coat at $t = 40.0$ s. In order to observe the internal 3D spatial distribution of the crack sources more intuitively, the non-failure elements of the top coat are deliberately hidden; only the bond coat and the failed elements of the top coat are displayed and portrayed in different colors. It is evident that several microcracks appear simultaneously at the TC/BC interface (Crack Source I) or inside the top coat (Crack Source II).

Nevertheless, it seems that the distribution of the microcracks inside the top coat (Crack Source II) is random and even. For further study, slices perpendicular to the z -axis (marked as “A”, “B”, “C”, and “D”) are taken from the model to observe the exact location of the microcracks (Fig. 12). The partial enlargements show that these failed elements are located just along the pore boundaries. Fig. 13 shows the first principal stress contour of the 3D FE model at $t = 30.0$ s. It is found that stress concentration mainly occurs at the TC/BC interface or along the pore boundaries, which are generally regarded as weak regions of the coatings. Obviously, it is the local, relatively high, concentrated stress that leads to the failure of the elements of the top coat, thus inducing the development of multiple crack sources.

4.2.2. Evolution of the primary crack

The formation and propagation of the primary crack inside the top coat are shown in Fig. 14. At time $t = 44.4$ s from initial application of the load, the generated microcracks at the TC/BC interface [labeled as “I”, “II”, “III”, and “IV”, see Fig. 14(a)] propagate, amalgamate, and begin to form a primary crack, as shown in Fig. 14(b). This moment

corresponds to the peak value of internal energy shown in Fig. 8. The inset in Fig. 14(b) displays the first principle stress vectors at the crack tip; tensile stress in the z -direction can be seen very clearly. As a result, the primary crack propagates horizontally inside the top coat along the interface direction, that is, normal to the vertical tensile stress. The specific crack propagation path is illustrated in Fig. 14(c).

As the applied load continues to increase, the primary crack propagates rapidly until the final spallation of the TBC. It is noted that at the later stage of loading, the primary crack will terminate at a TC/BC interface where the bond coat is an obvious convex above the surrounding surface. In this case, the crack prefers to propagate around the convex bond coat, as illustrated in Fig. 15, thus eventually inducing an undulating fracture morphology.

5. Conclusions

In this study, a 3D microscopic structural model reflecting the actual interface morphology and pore distribution of TBCs was built using micro-CT for the first time. The model was then applied to investigate

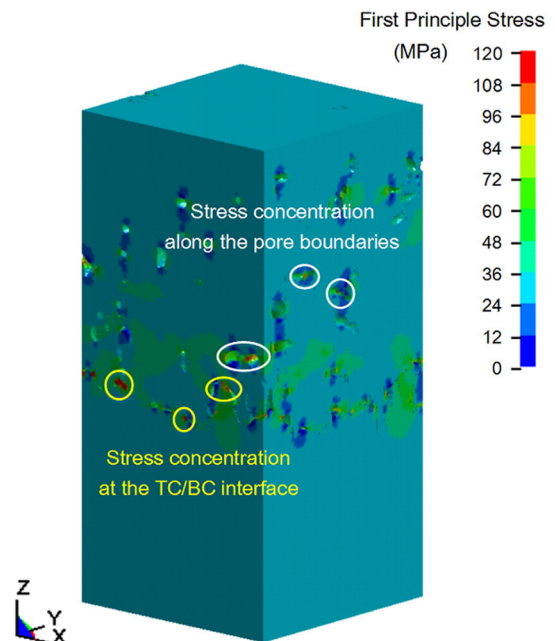


Fig. 13. The first principal stress contour of the FE model at $t = 30.0$ s.

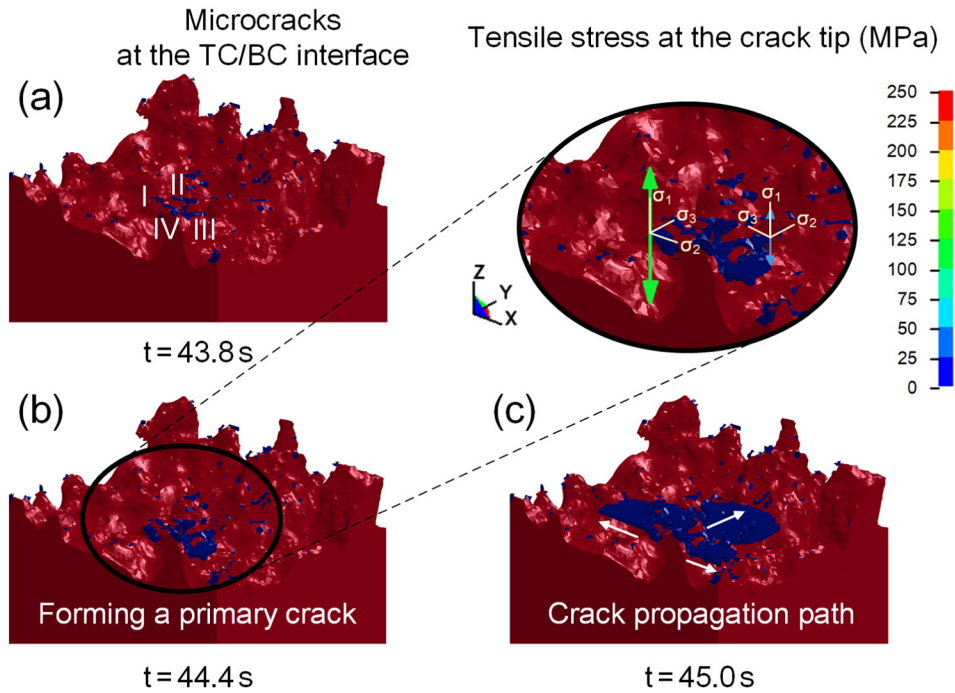


Fig. 14. Initiation and propagation of the primary crack: (a) microcracks at the TC/BC interface, (b) formation of the primary crack, and (c) propagation of the primary crack.

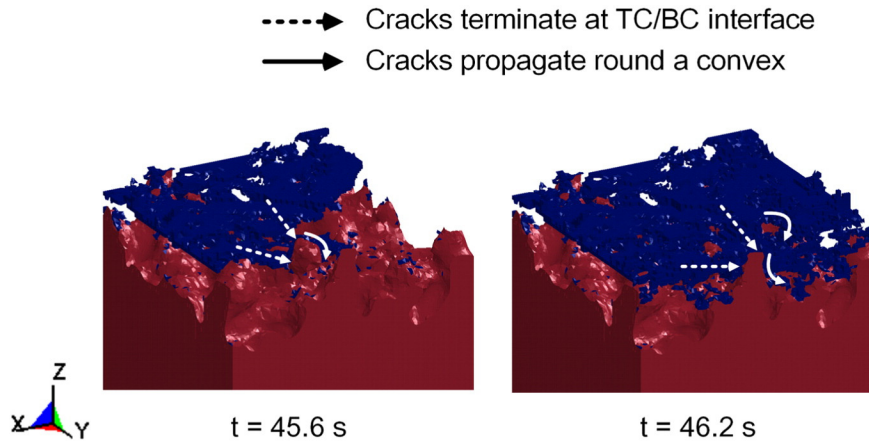


Fig. 15. Further propagation of the primary crack.

the 3D spatial evolution processes of damage and failure under uniaxial tension using FE techniques. To validate the numerical simulation results, the tensile responses of the TBCs were measured and a follow-up quantitative description of the tensile fracture morphology was obtained with a 3D surface profiler. The simulation results were in good agreement with the experimental data. The crack initiation and propagation path in 3D space was clearly observed and some compelling conclusions are drawn:

- (1) In the earlier stage of loading, local stress concentration induces two types of crack sources located either at the TC/BC interface or along the pore boundaries.
- (2) With the increase of load, only the crack sources at the interface amalgamate and begin to form a primary crack. This moment corresponds to the time of the peak value of the internal energy curve.
- (3) The primary crack propagates mainly along the TC/BC interface direction, i.e., normal to the vertical tensile stress at the crack tip.

- (4) At the later stage of loading, the primary crack terminates at the TC/BC interface and propagates around the convex bond coat until the final spallation of TBC.

Acknowledgments

We gratefully acknowledge the financial support of the Program for New Century Excellent Talents in University (NCET-12-0051).

References

- [1] C.V. Di Leo, J. Luk-Cyr, H.W. Liu, et al., A new methodology for characterizing traction–separation relations for interfacial delamination of thermal barrier coatings, *Acta Mater.* 71 (2014) 306–318.
- [2] W. Zhu, L. Yang, J.W. Guo, et al., Determination of interfacial adhesion energies of thermal barrier coatings by compression test combined with a cohesive zone finite element model, *Int. J. Plast.* 64 (2015) 76–87.

- [3] R. Ahmadi-Pidani, R. Shoja-Razavi, Improving the hot corrosion resistance of plasma sprayed ceria-yttria stabilized zirconia thermal barrier coatings by laser surface treatment, *Mater. Des.* 57 (2014) 336–341.
- [4] R. Vassen, G. Kerkhof, D. Stover, Development of a micromechanical life prediction model for plasma sprayed thermal barrier coatings, *Mater. Sci. Eng. A* 303 (2001) 100–109.
- [5] M. Azadi, G.H. Farrahi, G. Winter, et al., Damage prediction for un-coated and coated aluminum alloys under thermal and mechanical fatigue loadings based on a modified plastic strain energy approach, *Mater. Des.* 66 (2015) 587–595.
- [6] M. Mrdak, M. Rakin, B. Medjo, et al., Experimental study of insulating properties and behaviour of thermal barrier coating systems in thermo cyclic conditions, *Mater. Des.* 67 (2015) 337–343.
- [7] W. Shen, F.C. Wang, Q.B. Fan, et al., Finite element simulation of tensile bond strength of atmospheric plasma spraying thermal barrier coatings, *Surf. Coat. Technol.* 205 (2011) 2964–2969.
- [8] R. Xu, X.L. Fan, W.X. Zhang, et al., Effects of geometrical and material parameters of top and bond coats on the interfacial fracture in thermal barrier coating system, *Mater. Des.* 47 (2013) 566–574.
- [9] Z.B. Chen, Z.G. Wang, S.J. Zhu, Tensile fracture behavior of thermal barrier coatings on superalloy, *Surf. Coat. Technol.* 205 (2011) 3931–3938.
- [10] D.J. Wu, W.G. Mao, Y.C. Zhou, Digital image correlation approach to cracking and decohesion in a brittle coating/ductile substrate system, *Appl. Surf. Sci.* 257 (2011) 6040–6043.
- [11] Y.C. Zhou, T. Tonomori, A. Yoshida, et al., Fracture characteristics of thermal barrier coatings after tensile and bending tests, *Surf. Coat. Technol.* 157 (2002) 118–127.
- [12] X. Wang, S. Tint, M. Chiu, et al., Stiffness of free-standing thermal barrier coating top coats measured by bending tests, *Acta Mater.* 60 (2012) 3247–3258.
- [13] P.F. Zhao, C.A. Sun, X.Y. Zhu, et al., Fracture toughness measurements of plasma-sprayed thermal barrier coatings using a modified four-point bending method, *Surf. Coat. Technol.* 204 (2010) 4066–4074.
- [14] K. Loeffel, L. Anand, A chemo-thermo-mechanically coupled theory for elastic-viscoplastic deformation, diffusion, and volumetric swelling due to a chemical reaction, *Int. J. Plast.* 27 (2011) 1409–1431.
- [15] R.R. Balokhonov, V.A. Romanova, The effect of the irregular interface geometry in deformation and fracture of a steel substrate–boride coating composite, *Int. J. Plast.* 25 (2009) 2025–2044.
- [16] M. Ranjbar-Far, J. Absi, G. Mariaux, Finite element modeling of the different failure mechanisms of a plasma sprayed thermal barrier coatings system, *J. Therm. Spray Technol.* 21 (2012) 1234–1244.
- [17] M. Bialas, Finite element analysis of stress distribution in thermal barrier coatings, *Surf. Coat. Technol.* 202 (2008) 6002–6010.
- [18] U. Hermosilla, M.S.A. Karunaratne, I.A. Jones, et al., Modelling the high temperature behaviour of TBCs using sequentially coupled microstructural–mechanical FE analyses, *Mater. Sci. Eng. A* 513–14 (2009) 302–310.
- [19] E.P. Busso, J. Lin, S. Sakurai, et al., A mechanistic study of oxidation-induced degradation in a plasma-sprayed thermal barrier coating system. Part I: model formulation, *Acta Mater.* 49 (2001) 1515–1528.
- [20] H.E. Evans, Oxidation failure of TBC systems: an assessment of mechanisms, *Surf. Coat. Technol.* 206 (2011) 1512–1521.
- [21] R. Vassen, S. Giesen, D. Stoeber, Lifetime of plasma-sprayed thermal barrier coatings: comparison of numerical and experimental results, *J. Therm. Spray Technol.* 18 (2009) 835–845.
- [22] W. Shen, F.C. Wang, Q.B. Fan, et al., Lifetime prediction of plasma-sprayed thermal barrier coating systems, *Surf. Coat. Technol.* 217 (2013) 39–45.
- [23] M.Y. He, J.W. Hutchinson, A.G. Evans, Simulation of stresses and delamination in a plasma-sprayed thermal barrier system upon thermal cycling, *Mater. Sci. Eng. A* 345 (2003) 172–178.
- [24] M. Jinnestrand, S. Sjostrand, Investigation by 3D FE simulations of delamination crack initiation in TBC caused by alumina growth, *Surf. Coat. Technol.* 135 (2001) 188–195.
- [25] K. Al-Athel, K. Loeffel, H.W. Liu, et al., Modeling decohesion of a top-coat from a thermally-growing oxide in a thermal barrier coating, *Surf. Coat. Technol.* 222 (2013) 68–78.
- [26] M.J. Pindera, J. Aboudi, S.M. Arnold, Analysis of the spallation mechanism suppression in plasma-sprayed TBCs through the use of heterogeneous bond coat architectures, *Int. J. Plast.* 21 (2005) 1061–1096.
- [27] G. Bolelli, A. Candeli, H. Koivuluoto, et al., Microstructure-based thermo-mechanical modelling of thermal spray coatings, *Mater. Des.* 73 (2015) 20–34.
- [28] M. Gupta, K. Skogsberg, P. Nylen, Influence of topcoat–bondcoat interface roughness on stresses and lifetime in thermal barrier coatings, *J. Therm. Spray Technol.* 23 (2014) 170–181.
- [29] L. Pawlowski, The relationship between structure and dielectric-properties in plasma-sprayed alumina coating, *Surf. Coat. Technol.* 35 (1998) 285–398.
- [30] S. Beauvais, V. Guipont, M. Jeandin, et al., Influence of defect orientation on electrical insulating properties of plasma-sprayed alumina coatings, *J. Electroceram.* 15 (2005) 65–74.
- [31] F. Beckmann, R. Grupp, A. Haibel, et al., In-situ synchrotron X-ray microtomography studies of microstructure and damage evolution in engineering materials, *Adv. Eng. Mater.* 9 (2007) 939–950.
- [32] O. Amsellem, F. Borit, D. Jeulin, et al., Three-dimensional simulation of porosity in plasma-sprayed alumina using microtomography and electrochemical impedance spectrometry for finite element modeling of properties, *J. Therm. Spray Technol.* 21 (2012) 193–201.
- [33] R. Saenger, D. Martin, C. Gabrielli, Electrochemical characterization of plasma sprayed WC–Co coatings by impedance techniques, *Surf. Coat. Technol.* 194 (2005) 335–343.
- [34] C. Liu, Q. Bi, A. Leyland, An electrochemical impedance spectroscopy study of the corrosion behaviour of PVD coated steels in 0.5 N NaCl aqueous solution: Part I. Establishment of equivalent circuits for EIS data modelling, *Corros. Sci.* 45 (2003) 1243–1256.
- [35] SkyScan NV, Aartselaar, Belgium <http://www.skyscan.be/>.
- [36] Simpleware Ltd., Exeter, UK <http://www.simpleware.com/>.
- [37] G.J. Li, X. Zhang, Q.B. Fan, et al., Simulation of damage and failure processes of interpenetrating SiC/Al composites subjected to dynamic compressive loading, *Acta Mater.* 78 (2014) 190–202.
- [38] L. Wang, Y. Wang, X.G. Sun, et al., Influence of pores on the surface microcompression mechanical response of thermal barrier coatings fabricated by atmospheric plasma spray–finite element simulation, *Appl. Surf. Sci.* 257 (2011) 2238–2249.
- [39] M. Han, J.H. Huang, S.H. Chen, Behavior and mechanism of the stress buffer effect of the inside ceramic layer to the top ceramic layer in a double-ceramic-layer thermal barrier coating, *Ceram. Int.* 40 (2014) 2901–2914.
- [40] A.M. Freborg, B.L. Ferguson, W.J. Brindley, et al., Modeling oxidation induced stresses in thermal barrier coatings, *Mater. Sci. Eng. A* 245 (1998) 182–190.
- [41] J. Jeong, H. Adib, G. Pluvinage, Proposal of new damage model for thermal shock based on dynamic fracture on the brittle materials, *J. Non-Cryst. Solids* 351 (2005) 2065–2075.